

ENSO Transition, Duration, and Amplitude Asymmetries: Role of the Nonlinear Wind Stress Coupling in a Conceptual Model

KIT-YAN CHOI

Princeton University, Princeton, New Jersey

GABRIEL A. VECCHI AND ANDREW T. WITTENBERG

Geophysical Fluid Dynamics Laboratory, and Princeton University, Princeton, New Jersey

(Manuscript received 18 January 2013, in final form 31 May 2013)

ABSTRACT

The El Niño–Southern Oscillation (ENSO) exhibits well-known asymmetries: 1) warm events are stronger than cold events, 2) strong warm events are more likely to be followed by cold events than vice versa, and 3) cold events are more persistent than warm events. Coupled GCM simulations, however, continue to underestimate many of these observed features.

To shed light on these asymmetries, the authors begin with a widely used delayed-oscillator conceptual model for ENSO and modify it so that wind stress anomalies depend more strongly on SST anomalies (SSTAs) during warm conditions, as is observed. Then the impact of this nonlinearity on ENSO is explored for three dynamical regimes: self-sustained oscillations, stochastically driven oscillations, and self-sustained oscillations disrupted by stochastic forcings. In all three regimes, the nonlinear air–sea coupling preferentially strengthens the feedbacks (both positive and delayed negative) during the ENSO warm phase—producing El Niños that grow to a larger amplitude and overshoot more rapidly and consistently into the opposite phase, than do the La Niñas. Finally, the modified oscillator is applied to observational records and to control simulations from two global coupled ocean–atmosphere–land–ice models [Geophysical Fluid Dynamics Laboratory Climate Model version 2.1 (GFDL CM2.1) and version 2.5 (GFDL CM2.5)] to elucidate the causes of their differing asymmetries.

1. Introduction

Fluctuations of the El Niño–Southern Oscillation (ENSO) involve coupled changes to the ocean and atmosphere. During the warm phase of ENSO, the prevailing easterly winds over the central Pacific weaken; these westerly wind anomalies advect warm surface water toward the east, reduce the zonal slope of the thermocline, and inhibit the upwelling of cold water in the eastern Pacific, which feeds back positively on the warming of surface water in the eastern Pacific and allows small perturbations to grow. This positive feedback is also known as the Bjerknes feedback (Bjerknes 1969). To first approximation, La Niña (the cold phase) anomalies are roughly the opposite of those of El Niño (Larkin and Harrison 2002, hereafter LH2002). Theories proposed

to explain the termination of El Niño (La Niña) and its transition into the opposite phase include the reflection of oceanic internal waves at the eastern and western boundaries (Suarez and Schopf 1988; Battisti and Hirst 1989, hereafter BH1989), recharge and discharge of equatorial warm water due to Sverdrup balance (Jin 1997), western Pacific wind-forced Kelvin waves (Weisberg and Wang 1997), and anomalous zonal temperature advection by oceanic currents (Picaut et al. 1997). These theories agree that oceanic adjustments result in delayed negative feedbacks that explain the turnabout between El Niño and La Niña, with simple models illustrating how these mechanisms can result in oscillatory behavior for ENSO. Although nonlinearity has been shown to impact the growth and decay of El Niño (Tziperman et al. 1997; Gebbie et al. 2007; Vecchi 2006; Vecchi and Harrison 2006), linear techniques that are widely used for studying ENSO, such as empirical orthogonal function (EOF) analysis and linear regression, tend to treat El Niño and La Niña as simple mirror images of each other.

Corresponding author address: Kit-Yan Choi, Princeton University, 201 Forrester Road, Princeton, NJ 08540.
E-mail: kityanc@princeton.edu

For all of the approximate symmetries of El Niño and La Niña events, considerable asymmetry does exist. Most noted in past literature is the amplitude asymmetry of ENSO, namely that El Niño tend to be stronger than La Niña (Burgers and Stephenson 1999). Several oceanic mechanisms have been proposed for this asymmetry: nonlinear dynamical heating (Jin et al. 2003; An and Jin 2004) and negative feedback owing to tropical instability waves that are stronger during La Niña (Wang and McPhaden 2000; Vialard et al. 2001). A common element of all of these proposed mechanisms is their inherent oceanic origin.

Other studies have drawn attention to the asymmetric atmospheric response to sea surface temperature changes. Kang and Kug (2002) studied a hybrid atmosphere–ocean coupled model and suggested that the relatively weaker sea surface temperature anomalies (SSTs) and shorter duration for La Niña are attributable to the westward shift of the wind stress anomalies (Hoerling et al. 1997). Philip and van Oldenborgh (2009) and Frauen and Dommenget (2010) found that a nonlinear zonal wind response to the opposite sign SST anomalies may have an important influence on the SST skewness in the eastern tropical Pacific. Dommenget et al. (2013) suggest that the skewness in SST is related to the asymmetries in the pattern shape and the time evolution of ENSO events that can be partially attributed to the nonlinear response of the zonal wind to SST anomalies. Nonlinear relationships between the seasonal cycle and ENSO as well as the origins of ENSO phase locking to the seasonal cycle were also studied (Harrison and Vecchi 1999; Galanti and Tziperman 2000; Tziperman et al. 1997; Galanti et al. 2002).

In addition to amplitude asymmetry, there are other differences in the evolution of El Niño and La Niña. LH2002 characterized differences in the life cycles of the warm and cold phases by examining the ENSO behavior phase by phase. In their appendix, LH2002 note that warm-to-cold transitions tend to occur within a single year, with the cold event emerging the year following the warm event. In contrast, cold-to-warm transitions occur over 1–3 years. Okumura and Deser (2010) also showed that there is a robust asymmetry in the duration of El Niño and La Niña in observations, with La Niña persisting longer, a feature also noted by Kessler (2002). Subsequently, Okumura et al. (2011) proposed that an asymmetric wind response due to delayed SST forcing in the Indian Ocean acts to prolong La Niña.

Various observational datasets of Pacific surface wind stress support the hypothesis that during ENSO the wind stress response to the SST anomalies is weaker in the cold phase than in the warm phase. Figure 1 shows regression coefficients of zonal wind stress anomalies onto

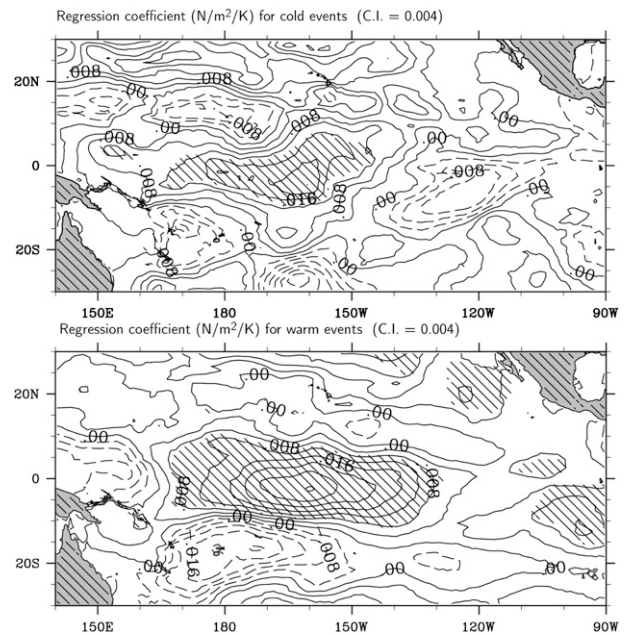


FIG. 1. Regression coefficient of FSU zonal wind stress anomalies onto the HadISST Niño-3.4 index for Niño-3.4 (top) greater than 0.5 K and (bottom) less than -0.5 K. Regions with confidence level exceeding 60% are hatched.

the Niño-3.4 SSTA index (area average of SST anomalies at 5°S – 5°N , 170° – 120°W) during warm and cold conditions for the Florida State University (FSU) observational wind product (see section 2). The asymmetry in the sensitivity is also evident in other estimates of wind stress. Figure 2 shows scatterplots of the zonal wind stress anomalies averaged over a 10° latitude by 40° longitude region where the regression coefficients are largest versus the observed Niño-3.4 SSTA index, from 2 months before an event peak to 2 months after the peak. The averaging area is also shifted zonally according to where the regression coefficients are largest for a particular ENSO phase. It is clear that wind stress responds more sensitively to sea surface temperature anomalies during warm conditions.

In this study, we have explored the impact of this atmospheric nonlinearity on the symmetry of ENSO. We will parameterize this effect in a simple model by having the air–sea coupling efficiency be dependent on the ENSO polarity and explore how this dependence can cause asymmetries in the duration, amplitude, and sequencing of ENSO. In section 2, we describe the observational datasets and GCM outputs to which we apply the measures described in section 3 to identify these three aspects of asymmetry. The formulation of the conceptual ENSO model used is given in section 3. The results are presented and analyzed in section 4. Section 5 gives a summary and further discussion.

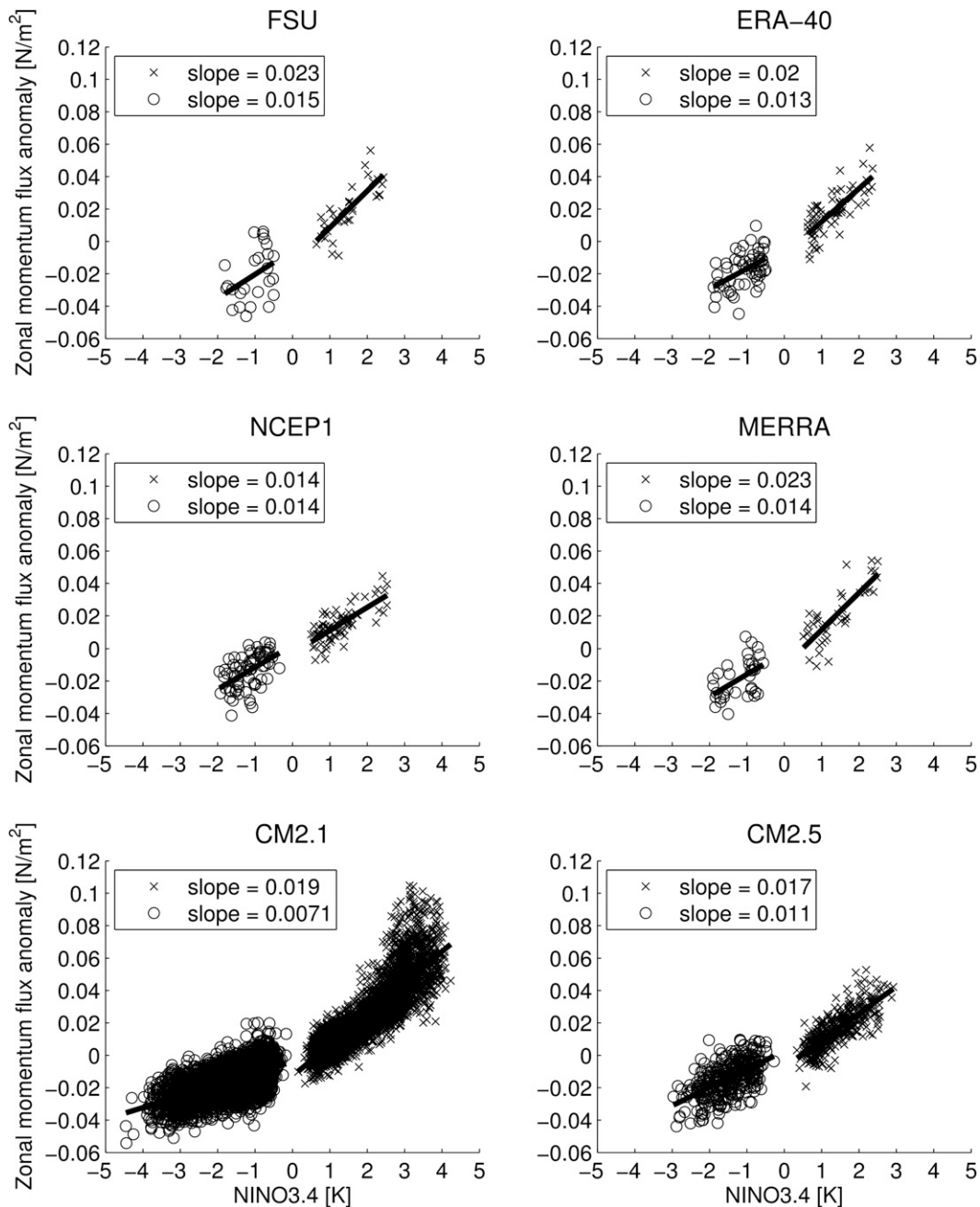


FIG. 2. Regression coefficient of the area-averaged zonal wind stress anomalies onto the Niño-3.4 (top) greater than 0.5 K or (bottom) less than -0.5 K. The HadISST Niño-3.4 index is used for the FSU and ERA-40 regression analysis. Reanalysis wind stress anomalies are regressed onto the reanalysis Niño-3.4 indices for MERRA and NCEP-1, respectively. Model wind stress anomalies are regressed onto the model Niño-3.4 index; area averages of the wind stress are computed within 40° longitude boxes from 5°S to 5°N where the regression coefficient is the largest across the equatorial Pacific domain. For warm events, wind stress anomalies are averaged within boxes at $177^\circ\text{--}137^\circ\text{W}$ (FSU), $176^\circ\text{--}144^\circ\text{W}$ (ERA-40), $176^\circ\text{--}136^\circ\text{W}$ (NCEP-1), $179^\circ\text{--}139^\circ\text{W}$ (MERRA), $167^\circ\text{--}153^\circ\text{W}$ (CM2.1), and $170^\circ\text{--}150^\circ\text{W}$ (CM2.5). For cold events, the box sits at $171^\circ\text{--}149^\circ\text{W}$ (FSU), $153^\circ\text{--}167^\circ\text{W}$ (ERA-40), $160^\circ\text{--}160^\circ\text{W}$ (NCEP-R1), $167^\circ\text{--}153^\circ\text{W}$ (MERRA), $140^\circ\text{--}180^\circ$ (CM2.1), and $140^\circ\text{--}180^\circ$ (CM2.5).

2. Data sources

a. SST data

There are uncertainties in past reconstructions of the tropical Pacific SST (Vecchi et al. 2008) and we therefore explore two SST datasets: the Hadley Centre Sea Ice and Sea Surface Temperature dataset (HadISST) and the extended reconstructed SST version 3b (ERSST).

1) HADISST

The HadISST dataset for 1880–2012 (Rayner et al. 2003) is used for computing the Niño-3.4 SSTA index. We examine the historical record entirely as well as in segments. Monthly climatologies are computed over the period of the time series sampled, and the anomalies are computed by subtracting the climatologies from the original record. The HadISST Niño-3.4 SST anomalies have increased by 0.2° from 1880 to 2012.

2) ERSST v3B

ERSST version 3b (Smith et al. 2008) provided by the National Oceanic and Atmospheric Administration is used as another long-term SST observational record to compare with HadISST. The dataset spans from 1854 to present. In the current study, the time series from 1880 to 2012 is used since the strength of the signal becomes more consistent after 1880. This version of SST analysis uses in situ SST data and improved statistical methods. Unlike version 3, satellite data, which that causes a small cold bias, is not used in version 3b. From 1880 to 2012, ERSST Niño-3.4 SST anomalies have increased by 0.6° .

The warming trends in the HadISST and ERSST products are included in the analysis presented below. The Niño-3.4 temperature anomalies are also smoothed using a running 5-month boxcar average before analysis. We will discuss the sensitivity of the results to whether the time series is detrended or not.

b. Surface wind stress estimates

There are also large uncertainties in reconstructions of wind stress over the Pacific (Wittenberg 2004), so we use multiple wind stress estimates in our analysis. Observational datasets used here for the wind stress response analysis are the Center for Ocean–Atmospheric Prediction Studies (COAPS) third-generation Florida State University objectively gridded Pacific monthly mean in situ flux products (FSU3) (Bourassa et al. 2005) from 1987 to 2004; the 40-yr European Centre for Medium-Range Weather Forecast (ECMWF) Re-Analysis (ERA-40) (Uppala et al. 2005) 6-hourly momentum stress product from September 1957 to August 2002; ECMWF Interim Re-Analysis (ERA-Interim) (Dee and Uppala 2009) from 1979 to 2011; the National Aeronautics and Space

Administration Modern-Era Retrospective Analysis for Research and Applications (MERRA) (Rienecker et al. 2011) from 1979 to 2010; and the National Centers for Environmental Prediction–National Center for Atmospheric Research (NCEP–NCAR) reanalysis (NCEP-1) (Kalnay et al. 1996; Kistler et al. 2001) from 1948 to 2011.

c. Coupled GCMs

1) GFDL CM2.1

The Geophysical Fluid Dynamics Laboratory (GFDL) Climate Model version 2.1 (CM2.1) is a global coupled atmosphere–ocean–land–ice GCM. The detailed formulations are described by Delworth et al. (2006, and references therein). Wittenberg et al. (2006) describes the behavior of ENSO in this model. The CM2.1 has taken part in phases 3 and 5 of the Coupled Model Intercomparison Project (CMIP3 and CMIP5) and the Fourth Assessment of the Intergovernmental Panel on Climate Change (IPCC). In this study, we use the monthly mean output of the preindustrial control experiment integrated for 4000 years with fixed 1860 estimates of solar irradiance, land cover, and atmospheric composition. The long run provides more than 300 El Niño and 300 La Niña events and thus allows statistically significant analysis of the behavior of the simulated ENSO. The description of the interdecadal variability of ENSO for the first 2200 years of this experiment is described in Wittenberg (2009).

2) GFDL CM2.5

The GFDL Climate Model version 2.5 (CM2.5) is a newer higher-resolution (atmosphere/land horizontal resolution is 0.5° instead of 2° ; ocean/sea ice resolution is about 0.25° instead of 1°) global coupled GCM based on CM2.1. The two models are initialized and forced in a similar fashion. The resolutions of the atmosphere and ocean components in CM2.5 are increased. A smaller viscosity is used in CM2.5. Parameterized eddy mixing is excluded in the CM2.5 ocean, while it is included in CM2.1. Further details on CM2.5 and comparisons with CM2.1 are documented in Delworth et al. (2012). The data used in this study are based on a 260-yr control experiment using fixed 1990 estimates of solar irradiance, land cover, and atmospheric composition. The 37 El Niños and 34 La Niñas are identified in this experiment.

3) COMPARISON OF THE SIMULATED ENSO IN CM2.5 AND CM2.1 WITH OBSERVATIONS

Delworth et al. (2012) describe how the simulated ENSO in CM2.5 compares to CM2.1 and observations. More detailed descriptions of the CM2.1 ENSO behavior can be found in Wittenberg et al. (2006). Here we summarize some of their results.

The ENSO amplitude in CM2.5 is weaker and is closer to observations, while CM2.1 tends to simulate ENSO events that are too strong. While both models have equatorial Pacific SST anomalies that extend too far to the west, this bias is reduced in CM2.5.

Both models have problems simulating the seasonal phase locking of ENSO. The CM2.1 ENSO shows almost no seasonal phase locking, except that the Niño-3.4 index has a slight tendency to peak between October and February and strong events tend to lock better to the seasonal cycle. The CM2.5 Niño-3.4 index has better phase locking compared to CM2.1 but is still weaker and later than observations by about a month.

At interannual time scales, the spectrum of tropical Pacific SSTs in CM2.5 is too concentrated at about 2.5 yr. CM2.1 shows a broader and more realistic spectrum but is stronger than the observations at interannual time scales. Accordingly, the ENSO in CM2.5 is noticeably more regular than CM2.1 and the observed. However, the lengths of observational records are short, so the spectra in this frequency band are uncertain (Wittenberg 2009; Vecchi and Wittenberg 2010).

3. Methods

a. The conceptual ENSO model

Following the delayed-oscillator model proposed by BH1989, which is closely related to the models studied by Suarez and Schopf (1988) and Zebiak and Cane (1987), we model ENSO as arriving from two essential drivers: first, the Bjerknes positive feedback that leads to instability and, second, a delayed negative feedback that results in oscillations. We thereby use a conceptual model of ENSO based on the BH1989 model:

$$\frac{\partial T}{\partial t} = -bT + c'\tau^x(t - t_1) - d'\tau^x(t - t_2) - \epsilon T^3, \quad (1)$$

where T is the Niño-3.4 SST anomaly; τ^x is the wind stress anomaly at the central equatorial Pacific near the date line; t_1 is the time required for wind stress response to positively feedback to surface temperature T ; t_2 is the time required for the negative feedback to enact; t_1 is smaller than t_2 ; b , c' and d' are positive scalar parameters; and ϵ is nonzero when the system is unstable otherwise. The current settings for t_1 and t_2 are 1 and 6 months, which are roughly the times required for the first/second baroclinic Kelvin wave to propagate eastward from the date line to the American coasts and the time required for Rossby waves to propagate westward and reflect back as Kelvin waves to the eastern Pacific (Harrison and Giese 1988; Harrison and Vecchi 1999). The qualitative conclusion is unchanged if different values of t_1 and t_2 are

used as long as $t_2 > t_1$. If $t_1 = 0$, one recovers the BH1989 formulation.

The first term on the rhs of Eq. (1) is a qualitative representation of local dampings of T due to air-sea fluxes, the mean zonal advection of the anomalous zonal temperature gradient, and the mean vertical advection of the anomalous temperature gradient that depends on T . Guided by BH1989 and regression analysis on these processes at the eastern Pacific, the value of b is kept fixed at 0.24 month^{-1} throughout the entire study.

The second and the third terms are the positive and the delayed-negative feedbacks. Each of these two terms incorporates the anomalous zonal advection of the mean zonal temperature gradient, (part of the) mean vertical advection of the anomalous vertical temperature gradient, and the anomalous vertical advection of the mean vertical temperature gradient.

By construction, Eq. (1) gives a symmetric oscillator in which warm and cold maxima have equal persistence, frequencies, and amplitudes. To break the symmetry, we write $\tau^x = \tau^x(T)$ such that the wind stress anomalies respond more sensitively to warm SST anomalies than to cold SST anomalies. For simplicity, we write τ^x as a piecewise linear function of T ; that is,

$$\tau^x = \gamma(T + r|T|), \quad (2)$$

where γ (Pa K^{-1}) and r (nondimensional) are both scalar parameters. For r positive and less than 1, wind stress anomalies are stronger for the same degree of positive T than negative T .

From the regression analysis of wind stress response to SST anomalies (Fig. 1), we can estimate r from the difference in the regression slopes:

$$r = \frac{s_w - s_c}{s_w + s_c}, \quad (3)$$

where s_w and s_c are the slopes for warm and cold events, respectively.

Table 1 summarizes the value of r estimated from different datasets. Most datasets produce an r of about 20% with the exception of NCEP-1. This agrees with the suggestion made by Wittenberg (2004) that FSU is recommended over NCEP-1 for extended studies of ENSO since the former dataset agrees better with other observations and updated analysis. Why the NCEP-1 does not show the nonlinear relationship between the zonal wind stress and SST during ENSO, as is seen in other datasets, is unclear.

In addition to the asymmetry in the intensity of the wind response, it is likely that the zonal shift in the wind stress patterns (Fig. 1) between El Niño and La Niña

TABLE 1. Values of r estimated from linear regression analysis between wind stress anomalies and Niño-3.4 SST anomaly index. The rows show the data sources for the Niño-3.4 SST anomaly index used in regressions. The columns show the data sources for the zonal wind stress anomalies.

	τ_x anomaly dataset				
	ERA-40	ERA-Interim	FSU	MERRA	NCEP
HadISST	0.21	0.12	0.21	0.19	-0.09
NCEP	—	—	—	—	0.00
MERRA	—	—	—	0.24	—
ERA-Interim	—	0.23	—	—	—
ERA40	0.24	—	—	—	—

may also be an important feature of ENSO (Kang and Kug 2002). However, we forgo investigation of pattern change effects in the present study in order to focus more intensely on the effects of the wind stress strength anomaly.

Further regression analysis of the wind stress response shows that CM2.1 has a large estimated value of $r \approx 46\%$, much higher than the observed. Conversely, CM2.5 has a smaller value of r ($=15\%$).

As in BH1989, there are two key regions in the parameter space: one being a stable region in which the oscillator is damped and another being an unstable region in which small perturbations in the oscillator grow to infinity. The unstable regime can be further divided into an oscillatory and a nonoscillatory regime. To sustain an oscillation for the stable region, a stochastic wind forcing is superimposed on τ^x . The stochastic forcing has an amplitude that is normally distributed with mean zero and a standard deviation σ (Pa) and has a decorrelation time of 0.2 months. For the unstable region, no stochastic forcing is added, but ϵ in Eq. (1) would be nonzero to stabilize the oscillation (BH1989). The stability characteristics across the parameter space are shown in Fig. 3. A few examples of the parameter regimes 1 and 2 are shown

in Fig. 4. Region 1 is the linearly stable, damped region with $\epsilon = 0$. Region 2 is the linearly unstable region but is nonlinearly stable using $\epsilon > 0$. Region 3 is unstable when $\epsilon = 0$; with $\epsilon > 0$, the oscillation dies quickly and converges to a constant nonzero value, which is far from the observed behavior. Regime 3 is not considered in the rest of this study.

With stochastic forcing, Eq. (2) becomes

$$\tau^x = \gamma(T + r|T|) + N(t), \tag{4}$$

where N is Gaussian white noise with zero mean and standard deviation σ . Eq. (1) can be written more compactly as

$$\begin{aligned} \frac{\partial T}{\partial t} = & -bT + c[T(t-t_1) + r|T(t-t_1)|] \\ & - d[T(t-t_2) + r|T(t-t_2)|] \\ & + c'N(t-t_1) - d'N(t-t_2) - \epsilon T^3, \end{aligned} \tag{5}$$

where $c = \gamma c'$ and $d = \gamma d'$ now have units of 1 month^{-1} . In region 1 σ is nonzero only unless otherwise specified; ϵ ($\epsilon > 0$) is nonzero only in regions 2 and 3. The values of σ and ϵ are tuned so that the simulated T has a standard deviation of roughly 0.8 K in order to be compared with the observations. The values of σ and ϵ do not alter qualitative conclusions of this paper regarding the asymmetry of the simulated ENSO.

Since the stochastic forcing is independent of T and the additional damping is an odd function of T , neither of these two functions should introduce asymmetries. Any asymmetry in this model will be attributable entirely to τ^x as a piecewise function of T . This permits a focused look at the impacts of this particular nonlinearity, as a foundation for future inclusion of other nonlinearities. In this paper, we present figures using $r = 0\%$ and $r = 60\%$ for apparent and clear comparisons;

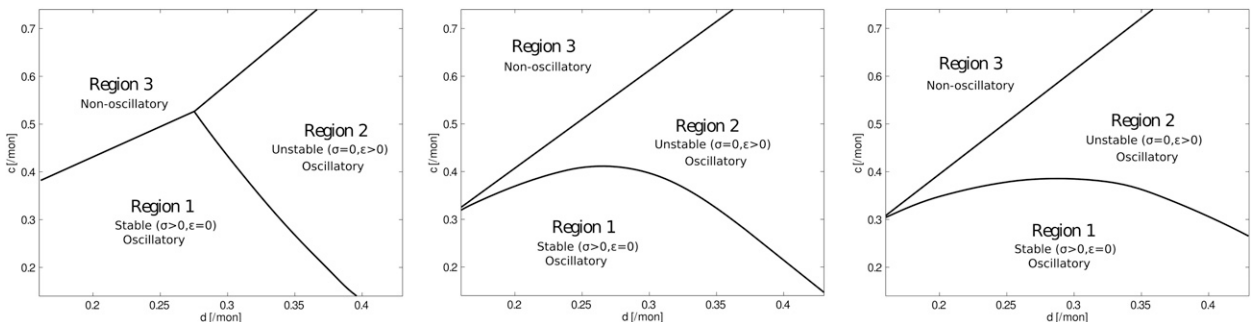


FIG. 3. Stability characteristics of the conceptual model in the c - d parameter space with $b = 0.24 \text{ month}^{-1}$ and (left) $r = 0$, (middle) $r = 20\%$, (right) $r = 60\%$. In Region 1 the system is linearly stable and sustained by normally distributed stochastic forcing ($\sigma > 0, \epsilon = 0$), and in Region 2 the system is linearly unstable but is limited by additional damping ($\epsilon > 0$); there is no stochastic forcing ($\sigma = 0$). Region 3 is unstable, nonoscillatory, and is not considered in the current study.

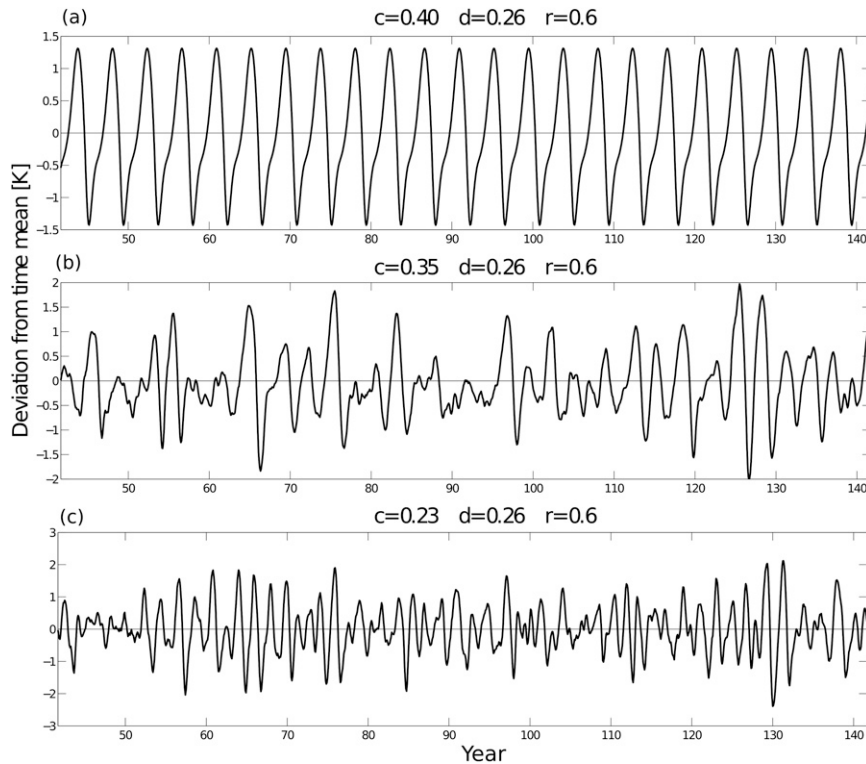


FIG. 4. Sample time series of temperature anomalies. Locations in the parameter space are shown in Fig. 11: (a) an example of self-sustained oscillations free of stochastic forcings and (b),(c) examples of stochastically driven oscillations in a stable system.

we have also explored other intermediate values of r and showed some results using $r = 20\%$ and $r = 40\%$.

b. Definitions of ENSO phases and asymmetry

To compare the conceptual model results with the observations and GCMs, consistent definitions of ENSO events, peaks, and durations are needed. Despite the richness of the ENSO phenomenon (e.g., LH2002; Wolter and Timlin 2011), we use the sea surface temperature anomaly in the central/eastern Pacific Ocean Niño-3.4 box as a proxy to illustrate the asymmetries of ENSO in observations and GCMs. To consistently compare the conceptual model results with the observations and GCMs, the same recipe is applied to the time series T simulated by the conceptual model.

El Niño (La Niña) is defined such that the 5-month running mean of the Niño-3.4 index exceeds (is below) its 90th (10th) percentile of the time series for at least three consecutive months. Other percentiles (e.g., 85th/15th) have been explored, and the fundamental results remain roughly the same. The years of warm and cold events in the observational datasets are summarized in Fig. 5. Figure 6 illustrates the criteria for defining events, terminations, and durations, as will be described below.

The termination time of events is calculated by the time lapse from the event peak to the time when the Niño-3.4 index first comes within 25% of the standard deviation from the time mean. If an event persists and reintensifies into another event of the same sign such that both events terminate at the same time, the preceding event is not considered in the duration analysis to avoid double counting.

The asymmetry in sequencing is examined by calculating the sample conditional probabilities of different types of transitions. This analysis is more uncertain for the observations largely due to the ambiguity of how one identifies a transition type and the inadequate number of events. To be consistent across observational datasets and GCM outputs, we adopt the following procedures when calculating the event transition probability:

- (i) identify the El Niño and La Niña events using the 90th and 10th percentiles and persistence criteria
- (ii) for each warm or cold event, for example, a warm event,
 - identify when the event terminates;
 - if the next event is a cold (warm) event and occurs within 12 months after the termination, this

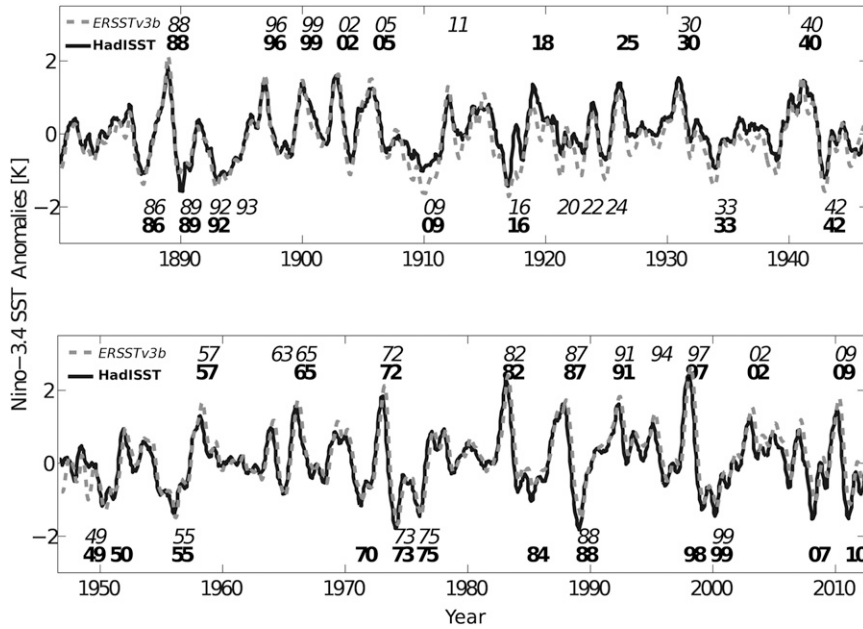


FIG. 5. Winter years of warm and cold events identified using the percentiles criteria on HadISST (solid line) and ERSSTv3b (dashed line) datasets. Numbers above (below) the time series indicate the years when warm (cold) events peak.

is identified as a warm-to-cold (warm-to-warm) transition.

Following these procedures, transition probabilities are calculated such that

$$P_{\text{warm-to-warm}} + P_{\text{warm-to-cold}} + P_{\text{warm-to-else}} = 1$$

$$P_{\text{cold-to-cold}} + P_{\text{cold-to-warm}} + P_{\text{cold-to-else}} = 1.$$

4. Results

a. Observations and GCM

In the observational record and the models, more warm events terminate within a year after peaks than

cold events do. Figure 7 shows the cumulative distribution of termination times for warm and cold events for the observational datasets and global-climate-model control run outputs. This result is consistent with LH2002 and Okumura and Deser (2010). If the Niño-3.4 SSTA time series is detrended, cold events appear to last much longer; that is, the asymmetry in duration is amplified upon detrending.

Following the procedures described in section 3, conditional probabilities for different transition types are calculated and shown in Fig. 8. From the observations, there is a higher likelihood to have warm events be followed by cold events than vice versa. Cold-to-cold transitions are also more frequent than warm-to-warm

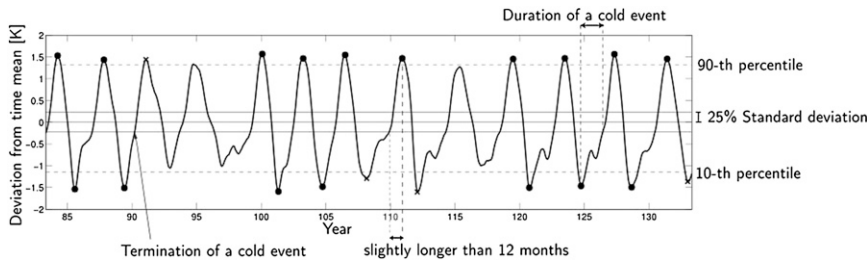


FIG. 6. A sample SST anomaly time series, filtered by 5-month running mean, illustrates how terminations, durations, and transitions are defined. The segment is simulated using the conceptual model with $b = 0.24 \text{ month}^{-1}$, $c = 0.49 \text{ month}^{-1}$, $d = 0.26 \text{ month}^{-1}$, $r = 0.6$, $\epsilon = 0.07 \text{ K}^2 \text{ month}^{-1}$, and $\sigma = 0.08\gamma \times 7 \text{ K} \approx 0.01 \text{ N m}^{-2}$ if $\gamma = 0.02 \text{ N m}^{-2} \text{ K}^{-1}$. Filled circles indicate event peaks followed by an event of the opposite sign. Crosses indicate event peaks that are not followed by an event, under the criteria described in section 3.

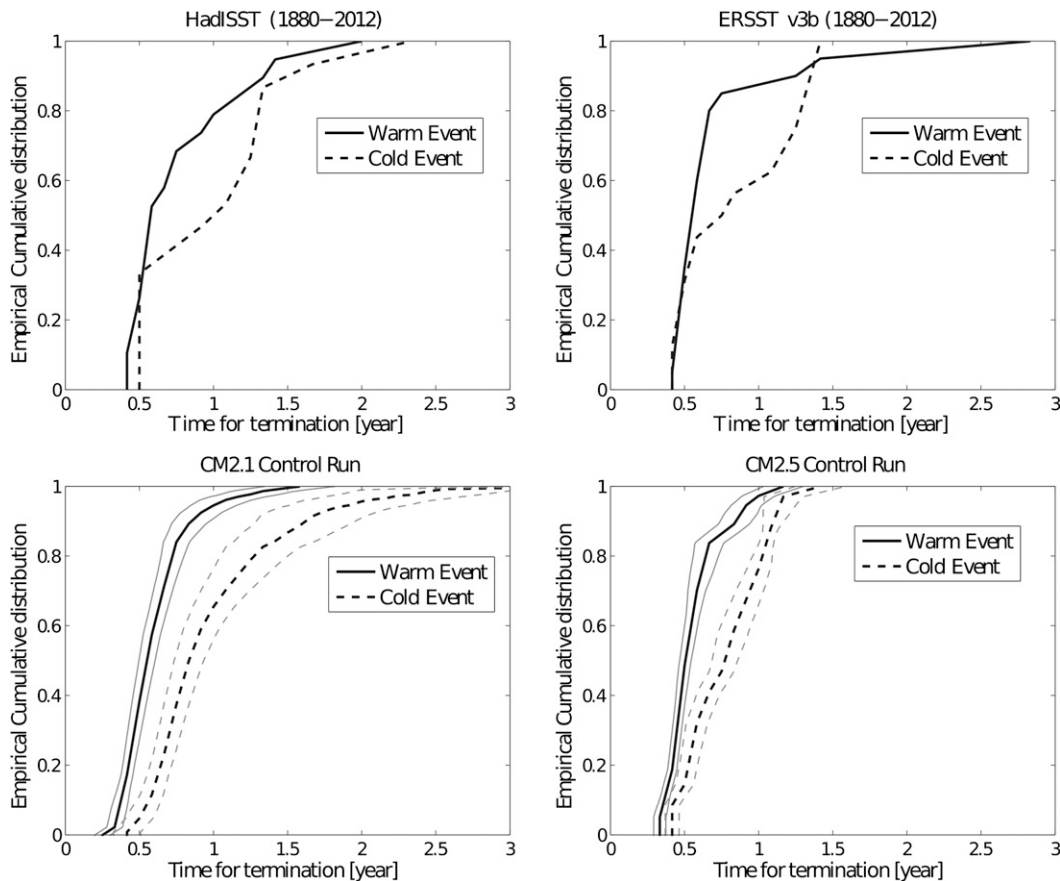


FIG. 7. Empirical cumulative distribution of event termination time using HadISST, ERSST, CM2.1, and CM2.5. The thick lines represent results using the entire time series, and, for the conceptual models, thin lines represent the standard deviation among 100-yr samples.

transitions. This qualitative conclusion holds even when a linear trend is removed from the Niño-3.4 SST index. The numbers of observed warm and cold events are so small that the statistical significance varies with the choice of Niño-3.4 SSTA thresholds as well as whether or not a linear trend is removed. In contrast, the control runs of CM2.1 and CM2.5 offer larger samples of El Niño and La Niña. The asymmetry in sequencing is consistently very strong in the CM2.1 control run, with warm-to-cold transitions much more likely than cold-to-warm transitions. CM2.5 shows an asymmetry in favor of warm-to-cold transitions that is weaker than in CM2.1 but is similar to the observations. Cold-to-cold transitions are very rare in both models.

Skewness is a useful measure to represent the amplitude asymmetry, as is summarized in Table 2. The Niño-3.4 SSTA index in the observations and CM2.1 have very consistent positive skewness, indicating stronger warm anomalies. CM2.5, however, with a more regular ENSO, shows a small negative skewness with the Niño-3.4 index and a small positive skewness with the Niño-3 index.

b. The conceptual ENSO model with $r > 0$

We have analyzed results using different values of r . Table 2 summarizes the asymmetries that the conceptual model is capable of at $r = 20\%$ and $r = 40\%$. Since more points in the c - d parameter space (i.e., fixing b) would show significant asymmetries with larger values of r , figures in this section present results using $r = 60\%$ for illustrative purposes. All qualitative results hold true for other positive values of r .

1) ASYMMETRY IN AMPLITUDE

Figure 9 shows the skewness across the c - d parameter space with $r = 60\%$. (The magnitude of the skewness increases with increasing values of r .) The skewness can be positive or negative depending on the relative strength of the positive and negative feedback, that is, the ratio of c and d . If c/d is large, extreme SST anomalies depend more on the instability brought by the positive feedback; that is, had the damping term been smaller, the system would be nonoscillatory and grow to

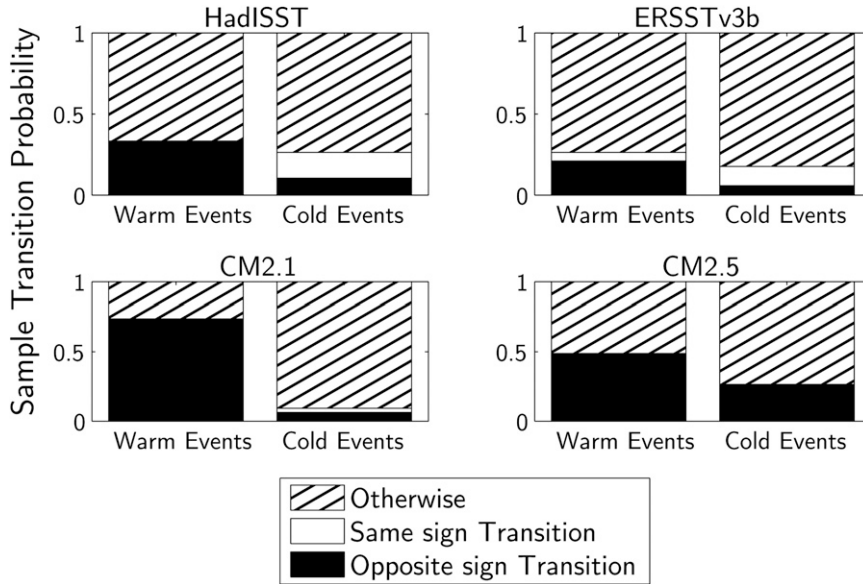


FIG. 8. Conditional probability of transitions for warm and cold events using the Niño-3.4 index.

infinity owing to the strong positive feedback. In this case, positive feedback is enhanced with a larger coupling efficiency during warm events. Therefore, warm events are able to grow to larger amplitudes while cold events become relatively weak, resulting in a positive skewness.

Instead, if d/c is large, extreme SST anomalies depend more on the strong overshooting of the preceding events of the opposite sign; that is, the system would be oscillatory unstable if the damping term was not strong enough. Therefore, cold events can grow to larger amplitudes owing to the stronger delayed cooling of the preceding warm events, while warm event peaks cannot grow as much since the delayed warming owing to the

preceding cold events is diminished. In short, if the coupling efficiency is larger during warm events, skewness becomes positive in the parameter region where positive feedback strength is large or negative where negative feedback strength is large. Notice that the cutoff does not lie along $c = d$ because b is nonzero.

2) ASYMMETRY IN DURATION

As r increases, cold events terminate at a later time than warm events do. This difference in termination times resembles the behavior found in the observations and GCMs. Figure 10 shows how the distributions of event termination time change with the value of r . The

TABLE 2. Parameters that produce the best simulations of observed, CM2.1, and CM2.5 asymmetry statistics. Parameter b is fixed at 0.24 month^{-1} , and r is also fixed at values based on the zonal wind stress analysis. Observations are Std: standard deviation of the temperature anomaly (K), Skewness: skewness of the temperature anomaly, LenDiff: termination time of cold events minus that of warm events (in months), and Pdiff: probability of warm-to-cold transitions minus that of cold-to-warm transitions. The row(s) below best fit correspond to the asymmetry statistics derived from the Niño-3.4 SSTA index. Parentheses represent statistics computed from the first and second halves of the Niño-3.4 SSTA index time series.

Observations								
	r	Std	Skewness	LenDiff	Pdiff	b	c	d
Best fit	0.2	0.7	0.26	0.52	0.43	0.24	0.37	0.24
HadISST		0.72 (0.68, 0.75)	0.34 (0.26, 0.43)	0.9 (-0.4, 2.9)	0.15 (0, 0.2)			
ERSST		0.77 (0.72, 0.79)	0.38 (0.35, 0.38)	2.1 (-1.1, 4.0)	0.11 (-0.1, 0.3)			
CM2.1								
Best fit	0.4	1.0	0.28	1.9	0.6	0.24	0.36	0.25
Niño-3.4		1.2	(0.28, 0.34)	(3.3, 3.4)	0.6			
CM2.5								
Best fit	0.2	1.1	-0.13	0.4	0.05	0.24	0.28	0.31
Niño-3.4		1.1	(-0.16, -0.06)	(2.2, 2.8)	0.11 (0.08, 0.12)			

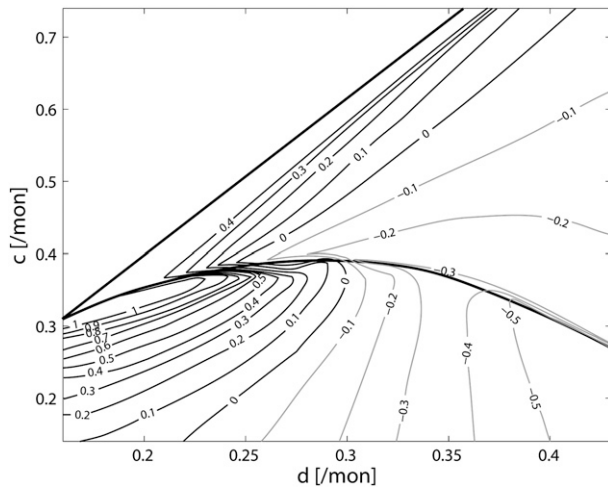


FIG. 9. Skewness of the simulated SST anomalies for the conceptual model with $r = 60\%$.

effect of $r > 0$ on the termination time across the parameter space is shown in Fig. 11.

Since the delayed negative feedback is strengthened for warm events, the warm events tend to terminate faster than cold events do. In addition, as a cold event decays more slowly, the temperature anomaly that precedes the eventual turnaround of the cold event is not as large as it would have been had the event decayed more rapidly. Therefore, the slower termination of cold events weakens the delayed warming and makes the termination even slower.

In addition, part of the longer termination time for cold events can be explained by the fact that the time mean state of the system is warmer than the equilibrium

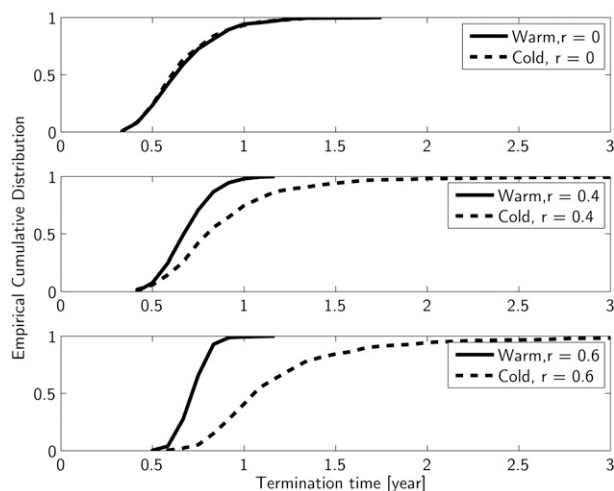


FIG. 10. Empirical cumulative distribution of event termination time for the conceptual model with values of $r = 0, 40\%, 60\%$ for $b = 0.24 \text{ month}^{-1}$, $c = 0.33 \text{ month}^{-1}$, and $d = 0.26 \text{ month}^{-1}$ (region 1).

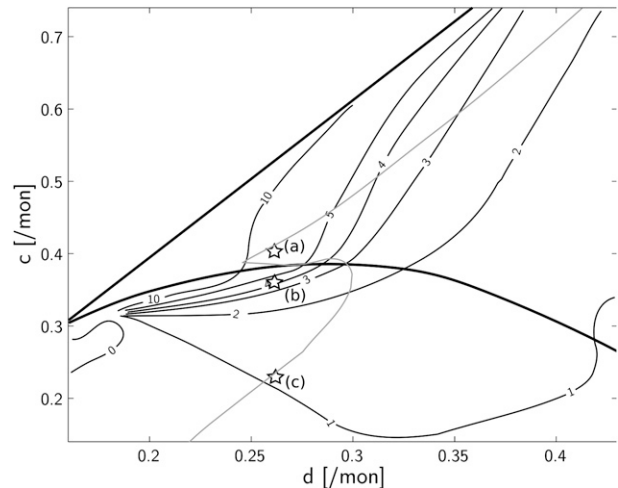


FIG. 11. Mean termination time (month) for cold events minus that for warm events in the conceptual model, with $r = 60\%$ and $b = 0.24 \text{ month}^{-1}$. The thick lines separate regions of different stability as in Fig. 3. Gray line is the zero skewness contour from Fig. 9. Star markers refer to sample temperature anomaly time series in Fig. 4.

state when the temperature anomaly is strongly positively skewed. Taking the warmer time mean state as the reference neutral state, as is done with the observational datasets, inevitably increases the termination time of cold events. Nevertheless, following the contour of zero skewness in Fig. 9, it is clear in Fig. 11 that cold events tend to last longer than warm events in the conceptual model even when there is little amplitude asymmetry.

If stochastic forcing is also added to self-sustained oscillations in region 2 (Fig. 12), the spread of the termination

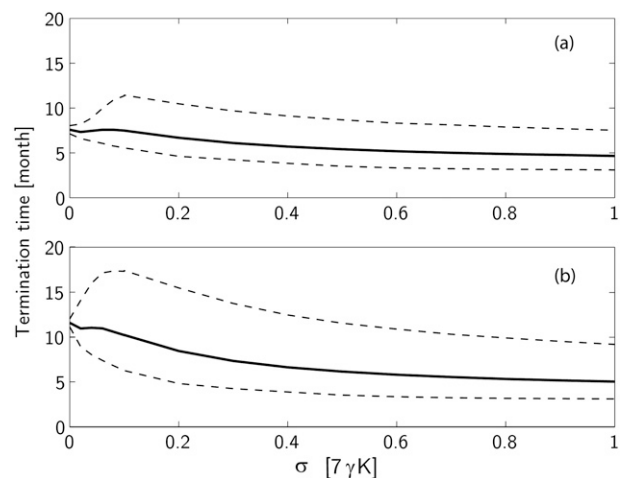


FIG. 12. Termination time for (a) warm and (b) cold events averaged across region 2 as a function of stochastic forcing amplitude with $r = 0.6$. Solid line represents the mean. Dashed lines represent the 95th and 5th percentiles of the termination time.

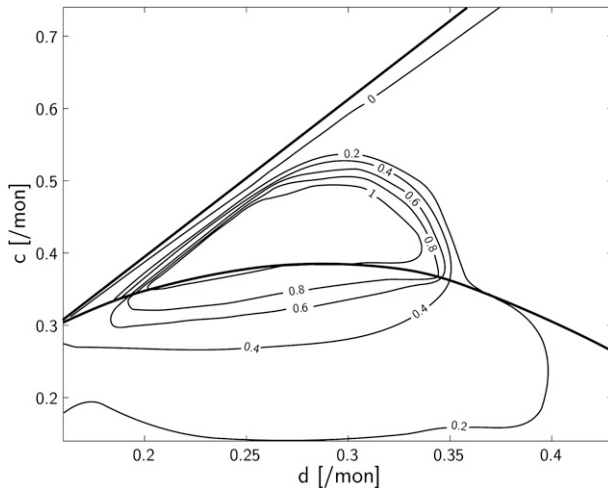


FIG. 13. Conditional probability of warm-to-cold transition minus that of cold-to-warm transitions for $r = 60\%$ across the c - d parameter space.

time distribution for cold events increases more than that for warm events. When the stochastic forcing intensity is moderate, high percentiles (e.g., 95th) of the cold event termination time extend more to longer durations than those of the warm events do. As stochastic forcing continues to amplify, the entire distribution of the termination time moves to shorter time scales because the signal begins to be dominated by stochastic forcing, which has higher frequencies than the ENSO. This result clearly illustrates the susceptibility of cold events to external forcing.

3) ASYMMETRY IN SEQUENCING

The conceptual model also shows a higher tendency for warm-to-cold transitions than cold-to-warm transitions with $r > 0$. As shown in Fig. 13, the probability of warm-to-cold transitions minus that of cold-to-warm transitions are positive everywhere in the stable and stochastically driven region (region 1). In region 2, the oscillation is self-sustained and is very regular. The positive difference in the transition probabilities in region 2, as shown in Fig. 13, is because some of the warm events peak later than 12 months after the preceding cold event termination and do not fulfill the transition criterion (see section 3).

If stochastic forcing is added to region 2, the probabilities of warm-to-warm and cold-to-cold transitions increase, and the latter increases more than the former, albeit to a slight extent (Fig. 14).

With the delayed negative feedback being stronger following warm events and weaker following cold events, warm events are more likely to be plunged into cold events than vice versa—since the cooling following warm

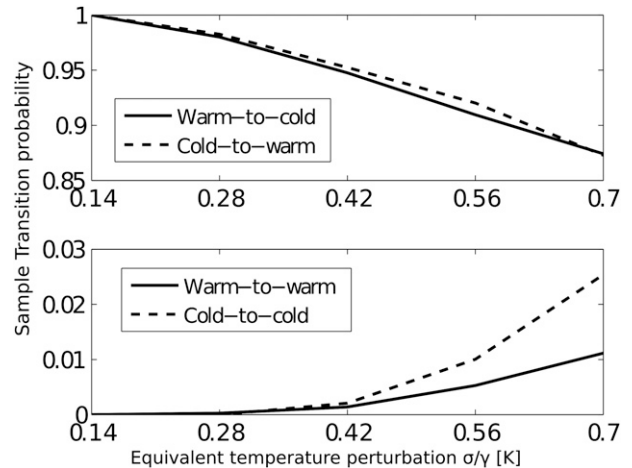


FIG. 14. Changes in transition probabilities with increasing stochastic forcing intensity and fixed $r = 60\%$ for region 2 (self-sustained oscillations). Results are averaged within the region that have $\text{probability}(\text{warm to cold}) = \text{probability}(\text{cold to warm}) = 1$ when stochastic forcing is absent.

events is strong enough to overshoot and is more resilient to disruptive stochastic forcing. In contrast, the weakened delayed warming during the termination of a cold event lowers the probability of a cold-to-warm transition. This explains why a stable, stochastically driven parameter region is necessary for the asymmetry in sequencing to be revealed in this conceptual model.

5. Summary and discussion

The asymmetries of ENSO were examined using observational records, coupled climate models, and a simplified dynamical framework. Three asymmetries between El Niño and La Niña are identified in models and observations: duration, sequencing, and amplitude. The duration asymmetry is the tendency of cold events to last longer than warm events do. The amplitude asymmetry involves warm events tending to be stronger. The sequencing asymmetry involves the tendency of warm events to be followed by cold events more readily than vice versa. The central equatorial Pacific wind stress anomalies also exhibit an asymmetric response to sea surface temperature anomalies in models and observations. Using the well-known delayed-oscillator conceptual model, we parameterize the impact of the zonal wind stress asymmetric response and demonstrate that this can lead to the aforementioned asymmetries in a consistent way. The duration asymmetry is pervasive across the parameter space that we have explored. The sequencing asymmetry can be obtained only if there is stochastic external forcing. The amplitude asymmetry has the same sign as that observed when the positive feedback is strong compared to the delayed negative feedback.

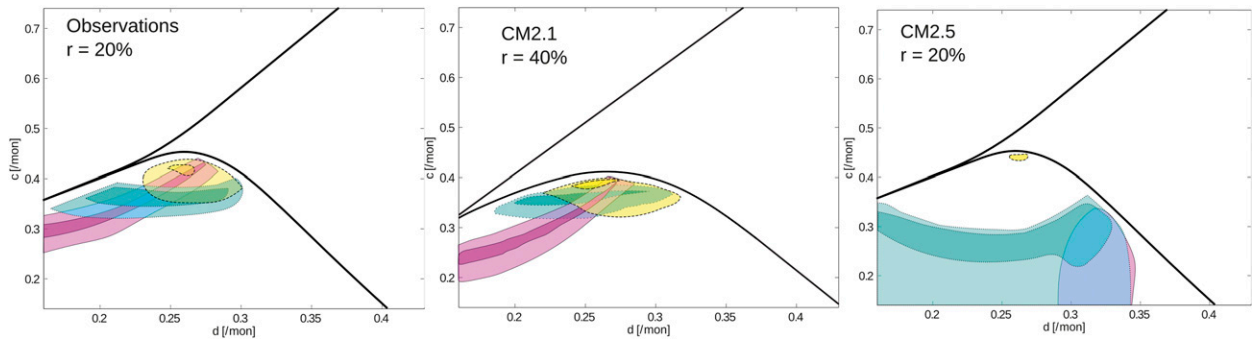


FIG. 15. Regions in the parameter space where the skewness (magenta, solid lines), warm-to-cold transition probability minus cold-to-warm transition probability (cyan, dotted line), and differences in termination time (yellow, dashed lines) are closest to the required values given by observations ($r = 20\%$), CM2.1 ($r = 40\%$), and CM2.5 ($r = 20\%$); see Table 2. Lighter (darker) regions correspond to errors less than 50% (less than 15%) of the targeted statistics.

The asymmetries owing to the additional nonlinearity to the ENSO conceptual model can be understood as follows: warm events are able to grow into larger amplitudes with the strengthened positive feedback. When they decay, the strengthened delayed negative feedback causes warm events to terminate faster and increases the chance of a following cold event. The initial growth of the cold events comes from the preceding warm event, but the cooling subsides soon after onset. If the overshooting is not too strong, the weakened positive feedback of cold events causes the cold events to mature at weaker amplitudes. When cold events terminate, the delayed negative feedback is weaker. The slower neutralization and the warmer long-term mean state are responsible for the longer durations of the cold events. Cold events are also more prone to be disrupted by external forcing and are less likely to be followed by a warm event. As a result, when there is a warm event, the predictability of a following cold event is higher. What follows a cold event is more uncertain. This result is consistent with Dommenges et al. (2013) that El Niños are mostly triggered by wind and are less predictable, while La Niñas are more predictable.

The conceptual model simplifies the system into a few feedback terms and provides a potential guide for investigations when a climate model simulates ENSO asymmetries that are too strong or too weak. Figure 15 shows the parameter space regions where the conceptual model resembles the asymmetry statistics of the observations, CM2.1, and CM2.5. Table 2 summarizes the best solutions and the corresponding asymmetries. We may conclude that the best solutions for the observations and CM2.1 are very close to each other. The fact that CM2.1 shows a stronger ENSO asymmetry may be explained by the larger r diagnosed for CM2.1. The negative skewness in CM2.5, on the contrary, can be explained by the stronger delayed negative feedback

parameter relative to that of the positive feedback. We speculate that the meridional extent of the wind stress anomaly may be the cause. Capotondi et al. (2006) show that the CMIP3 coupled GCMs exhibited a pervasive bias in which their patterns of wind stress anomalies were too far west and too narrow meridionally. They argued that, by amplifying the delayed negative feedback, this shortened the simulated ENSO period. The conceptual model suggests that, in the presence of asymmetric coupling ($r > 0$), in both models the narrow and westward-shifted wind stress response patterns could also help explain their tendency toward overly symmetric ENSO evolution. CM2.5, for example, has a particularly narrow wind stress anomaly pattern, a strong diagnosed delayed negative feedback, and highly symmetric ENSO behavior.

In the conceptual model, the difference in the wind stress response during warm and cold conditions also leads to a time mean state that is warmer than the equilibrium state. Since the equilibrium state of nature is unknown, computing anomalies from the climatology has been a conventional approach in analyzing ENSO strength and duration in observations and models. The time mean state, however, cannot be acquired a priori. Therefore, for applications in which the mean climate state is a necessary reference for analysis (e.g., in defining the onset or termination of an event), we suggest that the impact of changes in variability on the mean state be considered.

We also note that the seasonal cycle is not formally included in the current conceptual model. However, the nonlinear wind stress response to the SST anomaly is diagnosed from observations and coupled-climate-model control experiments in which the seasonal cycle is included. Therefore, the current results have not excluded, entirely, the contributions of the seasonal cycle on the asymmetry of ENSO.

The coupling efficiency dependence on the polarity of ENSO could have several causes. For example, observations indicate that westerly wind burst (WWB) occurrence depends on the state of ENSO (Harrison and Vecchi 1997; Vecchi and Harrison 2000). The state dependence of WWBs, their skewness, and their more frequent/strong occurrence at the onset of warm events would potentially be one of the processes that leads to a positive r , for example, through the low frequency component of the WWBs. GCM experiments also indicate that the frequency and intensity of WWB can be promoted during El Niño owing to a shifted location of the warmest water (Lengaigne et al. 2003). Eisenman et al. (2005) suggest that this state dependence may be equivalent to an increase in the air–sea coupling strength during El Niño events, and Gebbie et al. (2007) show that adding a state-dependent WWB parameterization to a hybrid coupled GCM increases the instability, irregularity, and asymmetry of its ENSO simulation.

The observational data for the wind stress responses suggests $r = 20\%$ for the conceptual model. While the model at $r = 20\%$ is capable of producing realistic asymmetries in amplitude and transition probability, the duration asymmetry is weaker than observed. This suggests that other sources of nonlinearities, such as nonlinear dynamical heating, the nonlinear relationship between the eastern Pacific thermocline depth and SST, and the nonlinear rectification of tropical instability waves, are also important in the understanding of the asymmetries.

The current study raises a number of questions: why is the wind stress response sensitivity stronger during warm events? Nonlinearities in atmospheric convection are a likely source. How important are atmospheric nonlinearities compared to oceanic nonlinearities? What are the roles of seasonality, ocean adjustment times, and the spatio-temporal patterns of wind stress coupling in the conceptual framework described here? How will future climate changes affect ENSO asymmetries? We are interested in answering these questions in the future.

Acknowledgments. We are indebted to Xiaosong Yang and Isaac Held for providing comments and suggestions. This report was prepared by KC under Award NA08OAR4320752 from the National Oceanic and Atmospheric Administration and U.S. Department of Commerce. The statements, findings, conclusions, and recommendations are those of the author(s) and do not necessarily reflect the views of the National Oceanic and Atmospheric Administration or the U.S. Department of Commerce.

REFERENCES

- An, S.-I., and F.-F. Jin, 2004: Nonlinearity and asymmetry of ENSO. *J. Climate*, **17**, 2399–2412.
- Battisti, D. S., and A. C. Hirst, 1989: Interannual variability in a tropical atmosphere–ocean model: Influence of the basic state, ocean geometry and nonlinearity. *J. Atmos. Sci.*, **46**, 1687–1712.
- Bjerknes, J., 1969: Atmospheric teleconnections from the equatorial Pacific. *Mon. Wea. Rev.*, **97**, 163–172.
- Bourassa, M. A., R. Romero, S. R. Smith, and J. J. O'Brien, 2005: A new FSU winds climatology. *J. Climate*, **18**, 3686–3698.
- Burgers, G., and D. B. Stephenson, 1999: The normality of El Niño. *Geophys. Res. Lett.*, **26**, 1027–1030.
- Capotondi, A., A. Wittenberg, and S. Masina, 2006: Spatial and temporal structure of tropical Pacific interannual variability in 20th century coupled simulations. *Ocean Modell.*, **15**, 274–298.
- Dee, D. P., and S. Uppala, 2009: Variational bias correction of satellite radiance data in the ERA-Interim reanalysis. *Quart. J. Roy. Meteor. Soc.*, **135**, 1830–1841.
- Delworth, T. L., and Coauthors, 2006: GFDL's CM2 global coupled climate models. Part I: Formulation and simulation characteristics. *J. Climate*, **19**, 643–674.
- , and Coauthors, 2012: Simulated climate and climate change in the GFDL CM2.5 high-resolution coupled climate model. *J. Climate*, **25**, 2755–2781.
- Dommenget, D., T. Bayr, and C. Frauen, 2013: Analysis of the nonlinearity in the pattern and time evolution of El Niño Southern Oscillation. *Climate Dyn.*, **40**, 2825–2847.
- Eisenman, I., L. Yu, and E. Tziperman, 2005: Westerly wind bursts: ENSO's tail rather than the dog? *J. Climate*, **18**, 5224–5238.
- Frauen, C., and D. Dommenget, 2010: El Niño and La Niña amplitude asymmetry caused by atmospheric feedbacks. *Geophys. Res. Lett.*, **37**, L18801, doi:10.1029/2010GL044444.
- Galanti, E., and E. Tziperman, 2000: ENSO's phase locking to the seasonal cycle in the fast-SST, fast-wave, and mixed-mode regimes. *J. Atmos. Sci.*, **57**, 2936–2950.
- , —, M. Harrison, A. Rosati, R. Giering, and Z. Sirkes, 2002: The equatorial thermocline outcropping—A seasonal control on the tropical Pacific ocean–atmosphere instability strength. *J. Climate*, **15**, 2721–2739.
- Gebbie, G., I. Eisenman, A. Wittenberg, and E. Tziperman, 2007: Modulation of westerly wind bursts by sea surface temperature: A semistochastic feedback for ENSO. *J. Atmos. Sci.*, **64**, 3281–3295.
- Harrison, D. E., and B. S. Giese, 1988: Remote westerly wind forcing of the eastern equatorial Pacific; some model results. *Geophys. Res. Lett.*, **15**, 804–807.
- , and G. A. Vecchi, 1997: Westerly wind events in the tropical Pacific, 1986–95. *J. Climate*, **10**, 3131–3156.
- , and —, 1999: On the termination of El Niño. *Geophys. Res. Lett.*, **26**, 1593–1596.
- Hoerling, M. P., A. Kumar, and M. Zhong, 1997: El Niño, La Niña, and the nonlinearity of their teleconnections. *J. Climate*, **10**, 1769–1786.
- Jin, F.-F., 1997: An equatorial ocean recharge paradigm for ENSO. Part I: Conceptual model. *J. Atmos. Sci.*, **54**, 811–829.
- , S.-I. An, A. Timmermann, and J. Zhao, 2003: Strong El Niño events and nonlinear dynamical heating. *Geophys. Res. Lett.*, **30**, 1120, doi:10.1029/2002GL016356.
- Kalnay, E., and Coauthors, 1996: The NCEP/NCAR 40-Year Reanalysis Project. *Bull. Amer. Meteor. Soc.*, **77**, 437–471.
- Kang, I.-S., and J.-S. Kug, 2002: El Niño and La Niña sea surface temperature anomalies: Asymmetry characteristics associated with their wind stress anomalies. *J. Geophys. Res.*, **107**, 4372, doi:10.1029/2001JD000393.
- Kessler, W. S., 2002: Is ENSO a cycle or a series of events? *Geophys. Res. Lett.*, **29**, 2125, doi:10.1029/2002GL015924.

- Kistler, R., and Coauthors, 2001: The NCEP-NCAR 50-Year Reanalysis: Monthly means CD-ROM and documentation. *Bull. Amer. Meteor. Soc.*, **82**, 247–267.
- Larkin, N. K., and D. E. Harrison, 2002: ENSO warm (El Niño) and cold (La Niña) event life cycles: Ocean surface anomaly patterns, their symmetries, asymmetries, and implications. *J. Climate*, **15**, 1118–1140.
- Lengaigne, M., J.-P. Boulanger, C. Menkes, G. Madec, P. Delecluse, E. Guilyardi, and J. Slingo, 2003: The March 1997 westerly wind event and the onset of the 1997/98 El Niño: Understanding the role of the atmospheric response. *J. Climate*, **16**, 3330–3343.
- Okumura, Y. M., and C. Deser, 2010: Asymmetry in the duration of El Niño and La Niña. *J. Climate*, **23**, 5826–5843.
- , M. Ohba, C. Deser, and H. Ueda, 2011: A proposed mechanism for the asymmetric duration of El Niño and La Niña. *J. Climate*, **24**, 3822–3829.
- Philip, S., and G. J. van Oldenborgh, 2009: Significant atmospheric nonlinearities in the ENSO cycle. *J. Climate*, **22**, 4014–4028.
- Picaut, J., F. Masia, and Y. D. Penhoat, 1997: An advective-reflective conceptual model for the oscillatory nature of the ENSO. *Science*, **277**, 663–666.
- Rayner, N. A., D. E. Parker, E. B. Horton, C. K. Folland, L. V. Alexander, D. P. Rowell, E. C. Kent, and A. Kaplan, 2003: Global analyses of sea surface temperature, sea ice, and night marine air temperature since the late nineteenth century. *J. Geophys. Res.*, **108**, 4407, doi:10.1029/2002JD002670.
- Rienecker, M. M., and Coauthors, 2011: MERRA: NASA's Modern-Era Retrospective Analysis for Research and Applications. *J. Climate*, **24**, 3624–3648.
- Smith, T. M., R. W. Reynolds, T. C. Peterson, and J. Lawrimore, 2008: Improvements to NOAA's historical merged land-ocean surface temperature analysis (1880–2006). *J. Climate*, **21**, 2283–2296.
- Suarez, M. J., and P. S. Schopf, 1988: A delayed action oscillator for ENSO. *J. Atmos. Sci.*, **45**, 3283–3287.
- Tziperman, E., S. E. Zebiak, and M. A. Cane, 1997: Mechanisms of seasonal-ENSO interaction. *J. Atmos. Sci.*, **54**, 61–71.
- Uppala, S. M., and Coauthors, 2005: The ERA-40 Re-Analysis. *Quart. J. Roy. Meteor. Soc.*, **131**, 2961–3012.
- Vecchi, G. A., 2006: The termination of the 1997–98 El Niño. Part II: Mechanisms of atmospheric change. *J. Climate*, **19**, 2647–2664.
- , and D. E. Harrison, 2000: Tropical Pacific sea surface temperature anomalies, El Niño, and equatorial westerly wind events. *J. Climate*, **13**, 1814–1830.
- , and —, 2006: The termination of the 1997–98 El Niño. Part I: Mechanisms of oceanic change. *J. Climate*, **19**, 2633–2646.
- , and A. T. Wittenberg, 2010: El Niño and our future climate: Where do we stand? *Wiley Interdiscip. Rev.: Climate Change*, **1**, 260–270.
- , A. Clement, and B. J. Soden, 2008: Examining the tropical Pacific's response to global warming. *Eos, Trans. Amer. Geophys. Union*, **89**, 81–83.
- Vialard, J., C. Menkes, J.-P. Boulanger, P. Delecluse, E. Guilyardi, M. J. McPhaden, and G. Madec, 2001: A model study of oceanic mechanisms affecting equatorial Pacific sea surface temperature during the 1997–98 El Niño. *J. Phys. Oceanogr.*, **31**, 1649–1675.
- Wang, W., and M. J. McPhaden, 2000: The surface-layer heat balance in the equatorial Pacific Ocean. Part II: Interannual variability. *J. Phys. Oceanogr.*, **30**, 2989–3008.
- Weisberg, R. H., and C. Wang, 1997: A western Pacific oscillator paradigm for the El Niño-Southern Oscillation. *Geophys. Res. Lett.*, **24**, 779–782.
- Wittenberg, A. T., 2004: Extended wind stress analyses for ENSO. *J. Climate*, **17**, 2526–2540.
- , 2009: Are historical records sufficient to constrain ENSO simulations? *Geophys. Res. Lett.*, **36**, L12702, doi:10.1029/2009GL038710.
- , A. Rosati, N.-C. Lau, and J. J. Plushay, 2006: GFDL's CM2 global coupled climate models. Part III: Tropical Pacific climate and ENSO. *J. Climate*, **19**, 698–722.
- Wolter, K., and M. S. Timlin, 2011: El Niño/Southern Oscillation behaviour since 1871 as diagnosed in an extended multivariate ENSO index (MEI.ext). *Int. J. Climatol.*, **31**, 1074–1087.
- Zebiak, S. E., and M. A. Cane, 1987: A model El Niño-Southern Oscillation. *Mon. Wea. Rev.*, **115**, 2262–2278.